ARMY RESEARCH LABORATORY

Development and Implementation of a Transversely Isotropic Hyperelastic Constitutive Model With Two Fiber Families to Represent Anisotropic Soft Biological Tissues

by Adam Sokolow and Samantha L. Wozniak

ARL-CR-738   June 2014

NOTICES

Disclaimers

The findings in this report are not to be construed as an official Department of the Army position unless so designated by other authorized documents.

Citation of manufacturer's or trade names does not constitute an official endorsement or approval of the use thereof.

Destroy this report when it is no longer needed. Do not return it to the originator.

Army Research Laboratory

Aberdeen Proving Ground, MD 21005-5066

Development and Implementation of a Transversely Isotropic Hyperelastic Constitutive Model With Two Fiber Families to Represent Anisotropic Soft Biological Tissues

Adam Sokolow

Oak Ridge Institute for Science and Education

Samantha L. Wozniak

Bowhead Science & Technology, LLC

prepared by

REPORT DOCUMENTATION PAGE

1. REPORT DATE *(DD-MM-YYYY)*	2. REPORT TYPE	3. DATES COVERED (From - To)
June 2014	Final	December 2013 – March 2014

4. TITLE AND SUBTITLE	5a. CONTRACT NUMBER
Development and Implementation of a Transversely Isotropic Hyperelastic Constitutive Model With Two Fiber Families to Represent Anisotropic Soft Biological Tissues	1120-1120-99/W911QX-09-C-0057
	5b. GRANT NUMBER
	5c. PROGRAM ELEMENT NUMBER

6. AUTHOR(S)	5d. PROJECT NUMBER
Adam Sokolow and Samantha L. Wozniak	
	5e. TASK NUMBER
	5f. WORK UNIT NUMBER

7. PERFORMING ORGANIZATION NAME(S) AND ADDRESS(ES)	8. PERFORMING ORGANIZATION REPORT NUMBER
ORAU Maryland 4692 Millennium Drive, Suite 101 Belcamp, MD 21017 Bowhead Science & Technology, LLC 403 Bata Blvd., Suite K Belcamp, MD 21017	ARL-CR-738

9. SPONSORING/MONITORING AGENCY NAME(S) AND ADDRESS(ES)	10. SPONSOR/MONITOR'S ACRONYM(S)
U.S. Army Research Laboratory ATTN: RDRL-WMP-B Aberdeen Proving Ground, MD 21005-5066	
	11. SPONSOR/MONITOR'S REPORT NUMBER(S)

12. DISTRIBUTION/AVAILABILITY STATEMENT

Approved for public release; distribution is unlimited.

13. SUPPLEMENTARY NOTES

14. ABSTRACT

We developed a transversely isotropic hyperelastic constitutive model to capture the anisotropy of the spinal intervertebral discs. The constitutive model was implemented in the finite element code SIERRA/SolidMechanics. This report documents the continuum theory of a transversely isotropic hyperelastic constitutive model with two fiber families and verifies the implementation of the numerical model on a variety of single element tests. The algorithm used to apply this model to spinal intervertebral discs is covered in depth, and an example simulation result is shown. Application of this model to other biological tissues, such as brain tissue and skeletal muscles, is also discussed.

15. SUBJECT TERMS

transversely isotropic hyperelastic, two fiber families, nearly incompressible, anisotropic, biological tissues

16. SECURITY CLASSIFICATION OF:			17. LIMITATION OF ABSTRACT	18. NUMBER OF PAGES	19a. NAME OF RESPONSIBLE PERSON
a. REPORT	b. ABSTRACT	c. THIS PAGE	UU	50	Adam Sokolow
Unclassified	Unclassified	Unclassified			19b. TELEPHONE NUMBER *(Include area code)* 410-306-2985

Contents

List of Figures

List of Tables

Acknowledgments

INTENTIONALLY LEFT BLANK.

1. Introduction

There is an increasing interest within the automotive, military, and clinical communities to use computer simulations to predict injury in humans. Researchers have developed finite element models of biological tissues and subjected their models to various loading conditions (*1–4*). Finite element models rely on accurate constitutive models of these tissues and therefore researchers must make critical decisions regarding the appropriate level of detail to include. While it is safe to assume anisotropy does exist in biological tissues, the role it plays during a high loading rate event, such as a blast, is not well understood. Numerical models that can turn these effects on or off are an incredibly useful tool.

The biological tissues that we consider here are soft and often have a high water content that places their bulk moduli close to that of water, i.e., around 2.3 GPa. However, they also typically have relatively low shear moduli, making them nearly incompressible. An extreme example is brain tissue where the lowest shear modulus values measured are around 2 kPa, cf. (*5–10*). Because these tissues have low shear moduli, they can reach extremely large shear strains making the nonlinear response of the tissues extremely important to characterize. These tissues typically are viscoelastic in nature as well; however, in this report we do not include rate-dependent behavior. Instead, we focus on the fibrous structures of soft tissues and how this structural anisotropy affects the mechanical behavior under different loading mechanisms.

This report introduces an anisotropic constitutive model for modeling the intervertebral discs of the spine. Since this type of model can be used for other soft biological tissues, we compromise between a fully general model and one that is overly specialized. Thus, the model is written in such a manner that it can be easily extended to capture the anisotropy of other biological tissues, such as brain or skeletal muscle. In this way, the constitutive model can be thought of as a numerical-analytical tool for investigating the mechanical response of fibrous tissue.

Section 2 introduces the background information relevant to intervertebral discs. Section 3 highlights the key points in the derivation of a transversely isotropic hyperelastic constitutive model with two fiber families. We then verify the implementation of the model in section 4. Section 5 describes an algorithm of how we incorporate the fiber directions for an intervertebral disc. Our future applications of the constitutive model as it will be applied to the spine, and could be applied to the brain and skeletal muscle, are discussed in section 6. Finally, our concluding remarks are presented in section 7.

2.   Structure and Biology of the Spine and Intervertebral Discs

The vertebral column, also known as the spine, is a bony structure comprised of vertebrae and intervertebral discs, stacked alternately on top of each other. As seen in figure 1a, five different regions make up the spine: the cervical spine, the thoracic spine, the lumbar spine, the sacrum and the coccyx. Each individual vertebra is named by referring to the first letter of their region (cervical, thoracic or lumbar), and, starting with the most superior (highest) vertebra in that region, numbered consecutively until the most inferior (lowest) vertebra in the region has been named.

Between each vertebra is a soft tissue called the intervertebral disc. The intervertebral discs play a major role in the motion of the spine by supporting compressive forces experienced during flexion (bending forward) and extension (bending backward), and resisting rotation, tension, and shear forces (*11*). An illustration of an intervertebral disc is shown in figure 1c. The intervertebral discs are made up of two main components: an inner gelatinous region, known as the nucleus pulposus (grey region), and an outer ring of fibrosus cartilage, known as the annulus fibrosus (white structures surrounding the grey region). The annulus fibrosus is composed of 15–25 concentric rings called lamellae (four rings are depicted in black in the figure) (*12, 13*). These rings consist of collagen fibers embedded within an extracellular matrix (alternating sets of diagonal lines). The orientation of the fibers varies between adjacent lamellae, alternating approximately $\pm 30°$ to the transverse plane of the disc.

Since the matrix of the annulus fibrosus is relatively soft, the fibers are believed to play a prominent role in the intervertebral disc's response to tensile (*14*) and shear loading. At the boundary between the vertebra and the intervertebral disc is a thin layer of semiporous bone, known as the vertebral endplate. The endplates of a healthy disc help absorb some of the pressure that results from mechanical loading of the spine and prevent the nucleus pulposus from bulging into the adjacent vertebra (*15*).

Over the past 60 years, there has been a substantial effort to model the spine and its individual components (*16*). Computational models of the spine provide researchers with an opportunity to gain a more detailed understanding of the deformation stress state and failure of the vertebrae and intervertebral discs. Typically, the annulus fibrosus is modeled in one of two ways: as a homogeneous composite of the matrix and the fibers or as an inhomogeneous composite of the matrix reinforced by collagen fibers (*17*). Shirazi-Adl found that representing the annulus

2

fibrosus as an inhomogeneous composite gave more realistic results and helped provide a better understanding of the biomechanical response of the intervertebral disc (*14*). Spring elements, truss elements, and rebar elements oriented at $\pm 30°$ to the transverse plane of the intervertebral disc have all been used by researchers to model the fibers of the annulus fibrosus (*1, 18–20*).
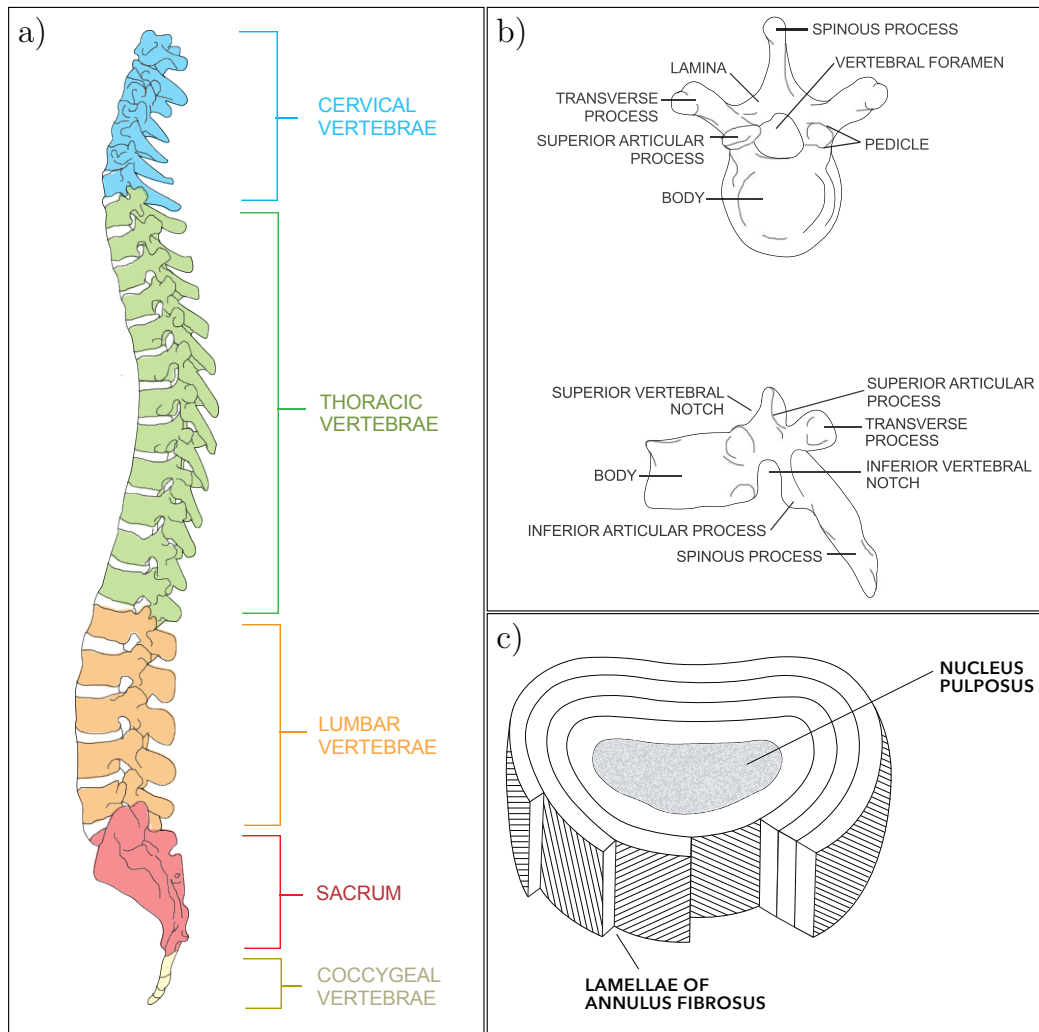
Figure 1. Bony anatomy of the spinal column (panel a) and a typical vertebra (panel b). Vertebra are color-coded according to their location classification. Panel c is an illustration (not drawn to scale) of an intervertebral disc showing the lamellar architecture of the annulus fibrosus (white) which surrounds the nucleus pulposus (grey). Some layers have been cut away from the annulus fibrosus to show the fiber network within the lamellae. Note that only four layers of lamellae are depicted in the figure but the annulus fibrosus usually has 15–25 layers. Collagen fibers (diagonal lines) are oriented at $\pm 30°$ to the transverse plane of the disc, with the direction alternating between adjacent lamellae in the annulus fibrosus.

3

3. Transversely Isotropic Hyperelastic Constitutive Model With Two Fiber Families

Soft tissues that are comprised of fibrous structures, such as muscles, ligaments, tendons, intervertebral discs and the brain, often exhibit strong anisotropy along these fiber directions (*21*). In this section, we provide the assumptions and physical arguments necessary for deriving a constitutive model for representing a fibrous material as a nearly incompressible, transversely isotropic hyperelastic material.

We largely follow the work set out by Weiss et al. (*22*), Holzapfel (*23*), Pinsky et al. (*24*), and Nguyen and Boyce (*25*). Instead of presenting a fully general model and then specializing it to our application, we introduce simplifying assumptions to tailor the derivation to our specific application. We make assumptions appropriate for a nearly incompressible, transversely isotropic hyperelastic material with up to two fiber families that do not interact with one another, nor the surrounding matrix, and whose response depends only on their stretch.

Let $\boldsymbol{F}$ be the deformation gradient describing the deformation of a material relative to some reference configuration. The polar decomposition of $\boldsymbol{F}$ is given by

$$\boldsymbol{F} = \boldsymbol{R}\boldsymbol{U} = \boldsymbol{V}\boldsymbol{R}, \tag{1}$$

and because $\boldsymbol{R}$ is a properly orthogonal rotation matrix, the eigenvalues of $\boldsymbol{F}$ are the same as those for $\boldsymbol{U}$ and $\boldsymbol{V}$, the right and left stretch tensors. These eigenvalues are also the principal stretches, which we denote as λ_i. We define the right and left Cauchy-Green deformation tensors, $\boldsymbol{C}$ and $\boldsymbol{B}$, respectively

$$\boldsymbol{C} \equiv \boldsymbol{F}^T\boldsymbol{F} \tag{2a}$$

$$\boldsymbol{B} \equiv \boldsymbol{F}\boldsymbol{F}^T \tag{2b}$$

which have the eigenvalues λ_i^2.

The ratio of the current specific volume to the reference specific volume is the Jacobian and is given by the determinant of the deformation gradient:

$$J \equiv \det \boldsymbol{F}. \tag{3}$$

The Jacobian allows us to define the *distortional part* of the deformation gradient:

$$\overline{\boldsymbol{F}} \equiv J^{-\frac{1}{3}}\boldsymbol{F} \tag{4}$$

The distortional part of the deformation gradient essentially normalizes the volume changes associated with the deformation and is denoted by a bar. This can be seen by taking the determinant of $\overline{\boldsymbol{F}}$:

$$\det\overline{\boldsymbol{F}} = \det(J^{-\frac{1}{3}}\boldsymbol{F}) = (J^{-1})\det(\boldsymbol{F}) = (J^{-1})(J) = 1\,. \tag{5}$$

We note that the eigenvalues of $\overline{\boldsymbol{F}}$ are $J^{-\frac{1}{3}}\lambda_i \equiv \overline{\lambda}_i$.

Analogous to the traditional approach in defining the right and left Cauchy-Green deformation tensors, we define the so-called *modified* right and left Cauchy-Green deformation tensors:

$$\overline{\boldsymbol{C}} \equiv \overline{\boldsymbol{F}}^T\overline{\boldsymbol{F}} \tag{6a}$$

$$\overline{\boldsymbol{B}} \equiv \overline{\boldsymbol{F}}\,\overline{\boldsymbol{F}}^T\,. \tag{6b}$$

The eigenvalues of $\overline{\boldsymbol{C}}$ and $\overline{\boldsymbol{B}}$ are $\overline{\lambda}_i^2$.

We next consider the invariants of the deformation tensors as they will be important for deriving our hyperelastic constitutive response from an energy density function. Let I_1, I_2, and I_3 denote the first three invariants of $\boldsymbol{C}$ and $\boldsymbol{B}$:

$$I_1 \equiv \operatorname{tr}\boldsymbol{C} = \operatorname{tr}\boldsymbol{B} \tag{7a}$$

$$I_2 \equiv \frac{1}{2}\left[(\operatorname{tr}\boldsymbol{C})^2 + \operatorname{tr}\boldsymbol{C}^2\right] = \frac{1}{2}\left[(\operatorname{tr}\boldsymbol{B})^2 + \operatorname{tr}\boldsymbol{B}^2\right] \tag{7b}$$

$$I_3 \equiv \det\boldsymbol{C} = \det\boldsymbol{B} = J^2 \tag{7c}$$

and $\overline{I}_1$, $\overline{I}_2$, and $\overline{I}_3$ the invariants of $\overline{\boldsymbol{C}}$ and $\overline{\boldsymbol{B}}$:

$$\overline{I}_1 \equiv \operatorname{tr}\overline{\boldsymbol{C}} = \operatorname{tr}\overline{\boldsymbol{B}} \tag{8a}$$

$$\overline{I}_2 \equiv \frac{1}{2}\left[(\operatorname{tr}\overline{\boldsymbol{C}})^2 + \operatorname{tr}\overline{\boldsymbol{C}}^2\right] = \frac{1}{2}\left[(\operatorname{tr}\overline{\boldsymbol{B}})^2 + \operatorname{tr}\overline{\boldsymbol{B}}^2\right] \tag{8b}$$

$$\overline{I}_3 \equiv \det\overline{\boldsymbol{C}} = \det\overline{\boldsymbol{B}} = 1\,. \tag{8c}$$

To incorporate anisotropy into our description, we define two fiber family directions in the reference configuration $\boldsymbol{a_0}$ and $\boldsymbol{g_0}$, with the property that $|\boldsymbol{a_0}| = 1$ and $|\boldsymbol{g_0}| = 1$. The

corresponding deformed fibers are given by applying the deformation gradient to the fiber direction in the reference configuration so that

$$a = Fa_0 , \quad \overline{a} = \overline{F}a_0 \tag{9a}$$

$$g = Fg_0 , \quad \overline{g} = \overline{F}g_0 . \tag{9b}$$

The lengths of the deformed fiber families are

$$\sqrt{a^T a} = \sqrt{(Fa_0)^T Fa_0} = \sqrt{a_0{}^T F^T Fa_0} = \sqrt{a_0{}^T Ca_0} \tag{10}$$

and since $|a_0| = 1$, the fiber stretch λ_a is

$$\lambda_a = \frac{\sqrt{a^T a}}{\sqrt{a_0{}^T a_0}} = \sqrt{a_0{}^T Ca_0} . \tag{11}$$

The same arguments can be made for the second fiber family, resulting in

$$\lambda_g = \sqrt{g_0{}^T Cg_0} . \tag{12}$$

Physical arguments, see for example, Weiss et al. (*22*) or Holzapfel (*23*), lead to the conclusion that the energy density function must depend on an even function of the fiber directions. Thus, one can conclude that the energy density function must depend on the structure tensor $a_0 \otimes a_0$ and $g_0 \otimes g_0$. For notational simplicity, let:

$$A_0 \equiv a_0 \otimes a_0 , \quad \text{and} \quad G_0 \equiv g_0 \otimes g_0 \tag{13}$$

and in the deformed configuration,

$$\overline{A} \equiv \overline{a} \otimes \overline{a} , \quad \text{and} \quad \overline{G} \equiv \overline{g} \otimes \overline{g} . \tag{14}$$

These additional tensors introduce additional *pseudo-invariants* of C, A_0, and G_0, which are

given by

$$I_4 \equiv \boldsymbol{a_0}^T \boldsymbol{C} \boldsymbol{a_0} = \lambda_a^2 \tag{15a}$$

$$I_5 \equiv \boldsymbol{a_0}^T \boldsymbol{C}^2 \boldsymbol{a_0} \tag{15b}$$

$$I_6 \equiv \boldsymbol{g_0}^T \boldsymbol{C} \boldsymbol{g_0} = \lambda_g^2 \tag{15c}$$

$$I_7 \equiv \boldsymbol{g_0}^T \boldsymbol{C}^2 \boldsymbol{g_0} \tag{15d}$$

$$I_8 \equiv \boldsymbol{a_0}^T \boldsymbol{C} \boldsymbol{g_0} \tag{15e}$$

$$I_9 \equiv \boldsymbol{a_0}^T \boldsymbol{g_0} \,. \tag{15f}$$

Similar expressions can be derived for the pseudo-invariants of the distortional tensors, but for reasons that will soon be clear we only include $\overline{I}_4$ and $\overline{I}_6$,

$$\overline{I}_4 \equiv \boldsymbol{a_0}^T \overline{\boldsymbol{C}} \boldsymbol{a_0} = J^{-\frac{2}{3}} \lambda_a^2 = \overline{\lambda}_a^2 \tag{16a}$$

$$\overline{I}_6 \equiv \boldsymbol{g_0}^T \overline{\boldsymbol{C}} \boldsymbol{g_0} = J^{-\frac{2}{3}} \lambda_g^2 = \overline{\lambda}_g^2 \,. \tag{16b}$$

The energy density function ϕ for a hyperelastic material is often written in terms of the right Cauchy-Green deformation tensor from which the second Piola-Kirchhoff stress tensor Σ can be determined,

$$\Sigma = 2 \frac{\partial \phi}{\partial \boldsymbol{C}} \,. \tag{17}$$

The energy density function can equivalently be thought of as some function of the first three invariants of either $\boldsymbol{C}$ or $\boldsymbol{B}$. Since the eigenvalues of $\boldsymbol{C}$ and $\overline{\boldsymbol{C}}$ or equivalently, $\boldsymbol{B}$ and $\overline{\boldsymbol{B}}$, are related by J, the energy density function can also be expressed in terms of the first three invariants of either $\overline{\boldsymbol{C}}$ or $\overline{\boldsymbol{B}}$. Thus, the motivation for introducing the modified deformation tensors is that the energy density can be written as some function of the Jacobian J and the modified right Cauchy-Green deformation tensor $\overline{\boldsymbol{C}}$, i.e.,

$$\phi = \overline{\phi}(J, \overline{\boldsymbol{C}}) \,. \tag{18}$$

Equivalently, the energy density must be some properly invariant function of the nine invariants previously discussed:

$$\phi = \overline{\phi}(J, \overline{I}_1, \overline{I}_2, \overline{I}_4, \overline{I}_5, \overline{I}_6, \overline{I}_7, \overline{I}_8, \overline{I}_9) \,, \tag{19}$$

where we've intentionally isolated out the dependence of $I_3 = J$. Since little is known about the actual constitutive response of these types of materials, a common simplification introduced is to assume that the fibers do not interact with one another. Thus, we assume that the mechanical

response is proportional to the first three isotropic invariants and only the stretches of the fiber families ($\bar{I}_4, \bar{I}_6$), i.e., assuming the energy density is a function of fewer parameters:

$$\phi = \bar{\phi}'(J, \bar{I}_1, \bar{I}_2, \bar{I}_4, \bar{I}_6) \, . \tag{20}$$

An additional simplification can be made when considering nearly incompressible materials. Typically for these soft materials, the energy density is decoupled into a spherical part (relating to pressures resulting from volume change) and a deviatoric response (shear response independent of volume changes). This is only approximately true for a real material since there will be coupling of pressure and shear terms at large deformations. This assumption decouples the energy density as follows:

$$\phi = \phi_s(J) + \phi_{\text{dev}}(\bar{I}_1, \bar{I}_2, \bar{I}_4, \bar{I}_6) \, . \tag{21}$$

where it can be shown that the pressure p is

$$p = -\frac{\partial \phi_s}{\partial J} \, , \tag{22}$$

and the deviatoric part of the Cauchy stress tensor $\text{dev}\,\boldsymbol{T}$ is

$$\text{dev}\,\boldsymbol{T} = \frac{2}{J}\text{dev}\left[\overline{\boldsymbol{F}}\frac{\partial \phi_{\text{dev}}}{\partial \overline{\boldsymbol{C}}}\overline{\boldsymbol{F}}^T\right] \, . \tag{23}$$

The partial derivative of the energy density with respect to the distortional part of the right Cauchy-Green tensor $\overline{\boldsymbol{C}}$ can be expanded using the chain rule. This procedure requires the following additional partial derivatives:

$$\frac{\partial \bar{I}_1}{\partial \overline{\boldsymbol{C}}} = \boldsymbol{I} \tag{24a}$$

$$\frac{\partial \bar{I}_2}{\partial \overline{\boldsymbol{C}}} = I_1 \boldsymbol{I} - \overline{\boldsymbol{C}} \tag{24b}$$

$$\frac{\partial \bar{I}_4}{\partial \overline{\boldsymbol{C}}} = \boldsymbol{A}_0 \tag{24c}$$

$$\frac{\partial \bar{I}_6}{\partial \overline{\boldsymbol{C}}} = \boldsymbol{G}_0 \, . \tag{24d}$$

Thus, the deviatoric part of the Cauchy stress can be written:

$$\text{dev}\,\boldsymbol{T} = \frac{2}{J}\text{dev}\left[\overline{\boldsymbol{F}}\left(\left(\frac{\partial \phi}{\partial \bar{I}_1} + \bar{I}_1\frac{\partial \phi}{\partial \bar{I}_2}\right)\boldsymbol{I} - \frac{\partial \phi}{\partial \bar{I}_2}\overline{\boldsymbol{C}} + \frac{\partial \phi}{\partial \bar{I}_4}\boldsymbol{A}_0 + \frac{\partial \phi}{\partial \bar{I}_6}\boldsymbol{G}_0\right)\overline{\boldsymbol{F}}^T\right] \, . \tag{25}$$

Multiplying through by $\overline{\boldsymbol{F}}$ on the left and its transpose $\overline{\boldsymbol{F}}^T$ on the right allows us to calculate the deviatoric part of the Cauchy stress in the reference configuration

$$\text{dev}\,\boldsymbol{T} = \frac{2}{J}\text{dev}\left[\left(\frac{\partial\phi}{\partial\overline{I}_1} + \overline{I}_1\frac{\partial\phi}{\partial\overline{I}_2}\right)\overline{\boldsymbol{B}} - \frac{\partial\phi}{\partial\overline{I}_2}\overline{\boldsymbol{B}}^2 + \frac{\partial\phi}{\partial\overline{I}_4}\overline{\boldsymbol{A}} + \frac{\partial\phi}{\partial\overline{I}_6}\overline{\boldsymbol{G}}\right]. \tag{26}$$

Following what has been done previously in the literature, we further assume that the isotropic response is that of the well known Mooney-Rivlin model, so that $\partial\phi/\partial\overline{I}_1 = C_{10}$ and $\partial\phi/\partial\overline{I}_2 = C_{01}$ are constants. We also assume that the stress response of both of the fiber families follow the same functional form, i.e., $\partial\phi/\partial\overline{I}_6 = \partial\phi/\partial\overline{I}_4 = \mathcal{F}(\overline{I})$, so that the deviatoric part of the Cauchy stress is

$$\text{dev}\,\boldsymbol{T} = \frac{2}{J}\text{dev}\left[\left(C_{10} + \overline{I}_1 C_{01}\right)\overline{\boldsymbol{B}} - C_{01}\overline{\boldsymbol{B}}^2 + \mathcal{F}(\overline{I}_4)\overline{\boldsymbol{A}} + \mathcal{F}(\overline{I}_6)\overline{\boldsymbol{G}}\right]. \tag{27}$$

As is typical for nearly incompressible materials, we assume the spherical part of the Cauchy stress to be

$$p = -\kappa\ln J\,, \tag{28}$$

where κ is the bulk modulus. Thus, the total Cauchy stress is given by:

$$\boldsymbol{T} = \kappa\ln J\boldsymbol{I} + \frac{2}{J}\text{dev}\left[\left(C_{10} + \overline{I}_1 C_{01}\right)\overline{\boldsymbol{B}} - C_{01}\overline{\boldsymbol{B}}^2 + \mathcal{F}(\overline{I}_4)\overline{\boldsymbol{A}} + \mathcal{F}(\overline{I}_6)\overline{\boldsymbol{G}}\right]. \tag{29}$$

We have intentionally avoided discussing the functional form of the fiber response and avoided writing down the hyperelastic energy density function explicitly. The choice of the fiber response depends on the biological tissue being modeled. In the literature, collagen fibers (*25*), as well as other fibers, have been modeled using an exponential function (*22, 24*). This gives a particular definition of the fiber response $\mathcal{F}$:

$$\mathcal{F}(\overline{I}) \equiv C_i\left(\exp\left[\beta_i(\overline{I} - 1)\right] - 1\right) \tag{30}$$

where the values of C_i and β_i can depend on the fiber family. The fiber response function takes the barred invariant $\overline{I}$ of a fiber family and returns the stress that results, thus, in practice, $\overline{I}$ in equation 30 will be either $\overline{I}_4$ or $\overline{I}_6$. While an energy density function can be written down for the case of equation 30, it may not be possible for all cases and functional forms of $\mathcal{F}$. An example of this might be including damage or dissipation to the fiber response. Section 6.3 discusses how this model can be extended to include a prestress and section 6.4 discusses an active contractile component that responds to applied strains.

4. Verification of Numerical Model

This section briefly covers various test cases to illustrate that our constitutive model has been implemented properly and behaves as expected. We conducted four simulations on a single element where we control the input fiber direction and the imposed deformation. The first three cases involve a single fiber family, and the fourth incorporates both fiber families. To ensure a set of rigorous tests, we considered compression, extension, and shear cases for a number of fiber family orientations. While closed-form solutions to each deformation were worked out using MuPad, they are too lengthy to be of any real analytical use. Instead, we compared our simulation results directly against the theoretically predicted responses in various figures where the angle of the fiber families vary between 0 and π.

In the first three tests, the initial fiber directions were taken so that the fiber had no component in the x, y, or z axis (corresponding to the planes YZ, XZ, and XY), respectively, i.e.,

$$\boldsymbol{a_0} = (0, \cos\theta, \sin\theta), \quad \boldsymbol{a_0} = (\cos\theta, 0, \sin\theta), \quad \text{or} \quad \boldsymbol{a_0} = (\cos\theta, \sin\theta, 0) \tag{31}$$

By sweeping θ from 0 to π, we tested cases for which the fiber direction was not along a principal axis of strain.

Table 1 lists the material parameters used in this verification. In the single fiber family cases, $C_g = 0$. These parameters were chosen because of their relevance to the soft intervertebral discs and to illustrate an important issue regarding the sensitivity of the fibers to numerical error (see shear test for a single fiber family). Additional tests (not shown here) further verified this model for additional choices of material parameters.

Table 1. Summary of material parameters used for the purpose of verifying the numerical model.

κ (MPa)	C_{10} (kPa)	C_{01} (kPa)	C_a (MPa)	β_a	C_g (MPa)	β_g
7.5	300	75	80	1	40*	1

*$C_g = 0$ in the single fiber family cases

4.1 Stretch and Compression Test for a Single Fiber Family

In these first two tests, the element is either stretched or compressed in the Z direction. The results of these test are shown in figures 2 and 3, respectively. In both cases, the physical components of the deformation gradient are given by

$$[\boldsymbol{F}] = \begin{bmatrix} 1 & 0 & 0 \\ 0 & 1 & 0 \\ 0 & 0 & \alpha \end{bmatrix}, \tag{32}$$

so that in compression $\alpha < 1$, and in tension $\alpha > 1$. In both cases, α is also the value of the Jacobian. Therefore, these tests also verify that the pressure response is implemented correctly.

It is important to note the fiber stretches that are predicted in each case. From equation 15a, the fourth pseudo-invariant is

$$\overline{I}_4 = \frac{a_x^2 + a_y^2 + \alpha^2\, a_z^2}{\alpha^{\frac{2}{3}}}, \tag{33}$$

so that in both the stretch and compression test

$$\overline{I}_4 = \frac{\cos\theta^2 + \alpha^2\,\sin\theta^2}{\alpha^{\frac{2}{3}}}, \quad \overline{I}_4 = \frac{\cos\theta^2 + \alpha^2\,\sin\theta^2}{\alpha^{\frac{2}{3}}}, \text{ or } \quad \overline{I}_4 = \frac{1}{\alpha^{\frac{2}{3}}}. \tag{34}$$

This implies that even for the case where the fiber has no z component, the fiber response will be a constant and independent of θ since equation 30 depends only on $\overline{I}_4$.* Figure 2 shows the results for the single fiber family stretch tests where $\alpha = 1.5$. The simulation results are shown as the symbols (x's) and the theoretical response as solid lines. Note that each symbol represents a separate single-element simulation with a unique fiber family orientation, so that 36 simulations are represented in each panel. Each component of the Cauchy stress $\boldsymbol{T}$ is represented by a unique color. The individual panels plot the stress as it depends on the angle θ, which specifies the undeformed fiber directions given by equation 31. The setup for figure 3 is the same, with the exception that $\alpha = 0.5$. Even at these large deformations, both figures 2 and 3 show excellent agreement between the numerical implementation of the constitutive model and the theoretical predictions regardless of the fiber plane or angle.

---

*Depending on the available experimental data and or the qualitative features desired from the model, equation 30 could be rewritten to depend on I_4 instead of $\overline{I}_4$ with minimal alterations to the code.

Figure 2. Single fiber family stretch test. Simulation (symbols) comparison against theoretical (solid lines) for the components of the Cauchy stress $\boldsymbol{T}_{xx}$ (red), $\boldsymbol{T}_{yy}$ (blue), $\boldsymbol{T}_{zz}$ (black), $\boldsymbol{T}_{xy}$ (cyan), $\boldsymbol{T}_{yz}$ (magenta), and $\boldsymbol{T}_{zx}$ (green) for three sets of fiber orientation vectors $\boldsymbol{a}_0$. Panel a shows the stress response of a single fiber family with initial direction vector in the YZ-plane. Similarly, panels b and c show a fiber family with initial direction vector in the XZ-plane, and XY-plane, respectively.
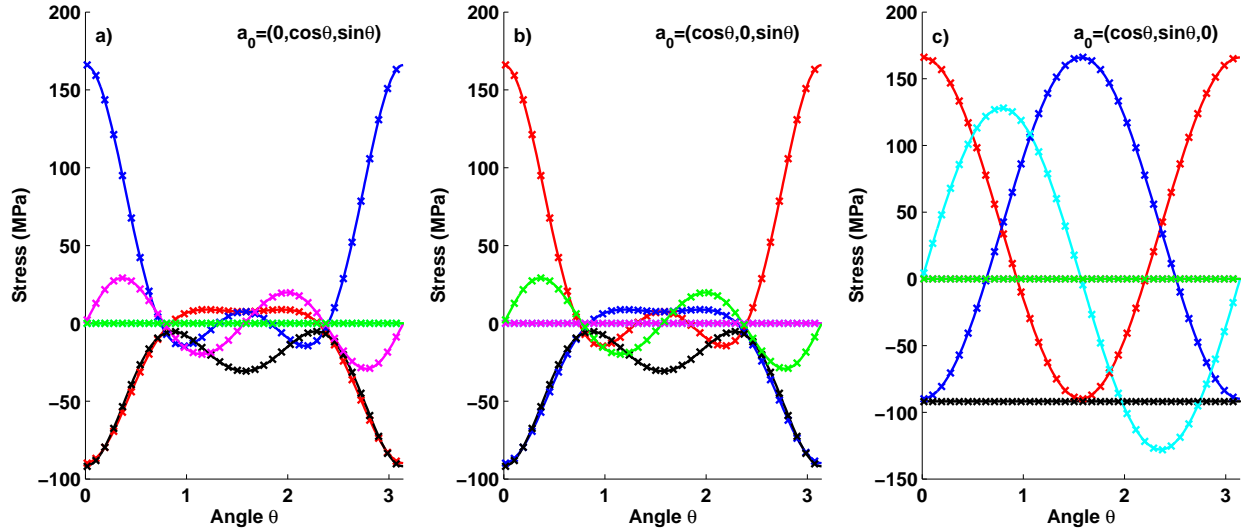
Figure 3. Single fiber family compression test. Simulation (symbols) comparison against theoretical (solid lines) for the components of the Cauchy stress $\boldsymbol{T}_{xx}$ (red), $\boldsymbol{T}_{yy}$ (blue), $\boldsymbol{T}_{zz}$ (black), $\boldsymbol{T}_{xy}$ (cyan), $\boldsymbol{T}_{yz}$ (magenta), and $\boldsymbol{T}_{zx}$ (green) for three sets of fiber orientation vectors $\boldsymbol{a}_0$. Panel a shows the stress response of a single fiber family with initial direction vector in the YZ-plane. Similarly, panels b and c show a fiber family with initial direction vector in the XZ-plane, and XY-plane, respectively.

12

4.2 Shear Test for a Single Fiber Family

The third case considered for the single fiber family was a shearing in the Y direction in the Z-plane (figure 4). In this case, the physical components of the deformation gradient are given by

$$[\boldsymbol{F}] = \begin{bmatrix} 1 & 0 & 0 \\ 0 & 1 & \alpha \\ 0 & 0 & 1 \end{bmatrix} . \tag{35}$$

Thus the fourth pseudo-invariant takes on the form

$$\bar{I}_4 = 1 + 2\alpha\, a_y\, a_z + \alpha^2\, a_z^2 \tag{36}$$

so that in each of the cases in equation 31:

$$\bar{I}_4 = 1 + 2\alpha\,\cos\theta\sin\theta + \alpha^2\,\sin\theta^2\,, \quad \bar{I}_4 = 1 + \alpha^2\,\sin\theta^2\,, \text{ or } \quad \bar{I}_4 = 1\,. \tag{37}$$

Figure 4 compares the simulation results for the single fiber family in shear. Panels a and b show excellent agreement between the theoretically predicted values and the simulation results. Panel c, however, shows some noteworthy deviations from the predicted theoretical curves. The deviation from the theoretical curves is an important issue to highlight and is entirely due to the small numerical error that SIERRA introduces in the rotation matrices during integration steps. Note that the scale bars in panel c are in kPa, while the other two panels are in MPa. Also note that for this specific example (see table 1), the choice of moduli place the isotropic response three orders in magnitude smaller than the fiber response. This particular test is an extreme case where the deformation leaves the fibers unchanged so that $\bar{I}_4$ should be unity and that by equation 30, the fiber response should be 0, leaving only the isotropic stress response. Upon closer inspection, the rotation matrices calculated by SIERRA had small errors when compared to the theoretically predicted values. In the pure shear case described previously, components of the left-Stretch tensor $\boldsymbol{V}$ and the rotation tensor $\boldsymbol{R}$ should be as follows:

$$[\boldsymbol{V}] = \begin{bmatrix} 1 & 0 & 0 \\ 0 & \frac{2+\alpha^2}{\sqrt{4+\alpha^2}} & \frac{\alpha}{\sqrt{4+\alpha^2}} \\ 0 & \frac{\alpha}{\sqrt{4+\alpha^2}} & \frac{2}{\sqrt{4+\alpha^2}} \end{bmatrix} , \quad [\boldsymbol{R}] = \begin{bmatrix} 1 & 0 & 0 \\ 0 & \frac{2}{\sqrt{4+\alpha^2}} & \frac{\alpha}{\sqrt{4+\alpha^2}} \\ 0 & -\frac{\alpha}{\sqrt{4+\alpha^2}} & \frac{2}{\sqrt{4+\alpha^2}} \end{bmatrix} . \tag{38}$$
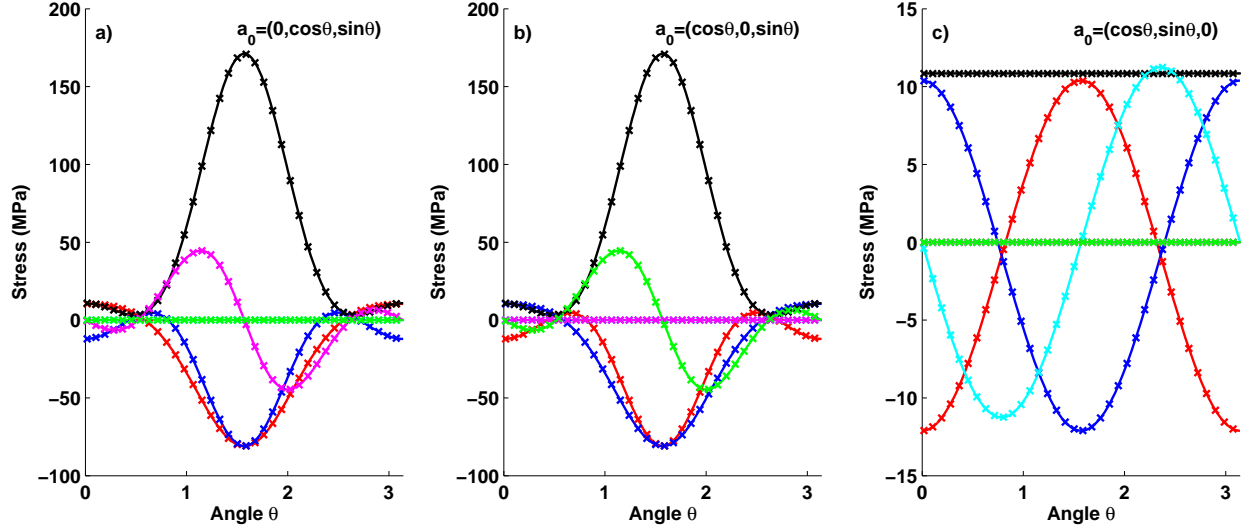
Figure 4. Single fiber family shear in Y-direction test. Simulation (symbols) comparison against theoretical (solid lines) for the components of the Cauchy stress $\boldsymbol{T}_{xx}$ (red), $\boldsymbol{T}_{yy}$ (blue), $\boldsymbol{T}_{zz}$ (black), $\boldsymbol{T}_{xy}$ (cyan), $\boldsymbol{T}_{yz}$ (magenta), and $\boldsymbol{T}_{zx}$ (green) for three sets of fiber orientation vectors $\boldsymbol{a}_0$. Panel a shows the stress response of a single fiber family with initial direction vector in the YZ-plane. Similarly, panels b and c show a fiber family with initial direction vector in the XZ-plane, and XY-plane, respectively.

In practice, however, we found even with strict demands on convergence criteria (in the implicit case) or small time steps (in the explicit case), the yy, yz, zy, and zz components of the actual tensors deviated from the theoretically predicted values

$$[\boldsymbol{V}_{\text{sim}}] \approx \begin{bmatrix} 1 & 0 & 0 \\ 0 & \frac{2+\alpha^2}{\sqrt{4+\alpha^2}} - \epsilon & \frac{\alpha}{\sqrt{4+\alpha^2}} + \epsilon/2 \\ 0 & \frac{\alpha}{\sqrt{4+\alpha^2}} + \epsilon/2 & \frac{2}{\sqrt{4+\alpha^2}} + \epsilon/2 \end{bmatrix}, \tag{39}$$

$$[\boldsymbol{R}_{\text{sim}}] \approx \begin{bmatrix} 1 & 0 & 0 \\ 0 & \frac{2}{\sqrt{4+\alpha^2}} - \epsilon/10 & \frac{\alpha}{\sqrt{4+\alpha^2}} - \epsilon/2 \\ 0 & -\frac{\alpha}{\sqrt{4+\alpha^2}} + \epsilon/2 & \frac{2}{\sqrt{4+\alpha^2}} + \epsilon/2 \end{bmatrix}. \tag{40}$$

We estimated ϵ from a few numerical simulations of the shear tests and found that its value typically was small, $\epsilon \approx 10^{-4}$. The product of $\boldsymbol{V}$ and $\boldsymbol{R}$ is $\boldsymbol{F}$, the deformation gradient, which to first order in ϵ is

$$[\boldsymbol{F}_{\text{sim}}] \approx \begin{bmatrix} 1 & 0 & 0 \\ 0 & 1 - \epsilon f_{yy}(\alpha) & \alpha - \epsilon f_{yz}(\alpha) \\ 0 & -\epsilon f_{zy}(\alpha) & 1 + \epsilon f_{zz}(\alpha) \end{bmatrix}, \tag{41}$$

14

where $f_{ij}(\alpha)$ are functions of the deformation. These functions were close to unity and their functional form is suppressed since they are not essential to the arguments that follow. Using this form of the deformation gradient, we can obtain an approximate expression for the fourth pseudo-invariant to the first order in ϵ:

$$\bar{I}_4 \approx 1 - \epsilon f(\alpha, \theta). \tag{42}$$

Inserting this expression into equation 30 gives

$$\mathcal{F}(\bar{I}_4) = C_3 \left[\exp(-\beta_a \epsilon f(\alpha, \theta)) - 1 \right] \approx -\epsilon C_3 \beta_a f(\alpha, \theta). \tag{43}$$

Using the values from table 1 and $\epsilon = 10^{-4}$ gives a fiber response, on the order of 10 kPa, whose magnitude will depend further on the deformation and the angle of the fiber. This is all of the same order as the error in figure 4c. Thus, the choice of an exponential function can make the simulation very sensitive to numerical error.

4.3 Compression Test With Two Fiber Families

The previous simulations were performed for single fiber families. The final verification of our implementation is a two fiber family test, in which we verify that the fiber families behave properly when both families are used. For this test, the fiber families are represented by the vectors:

$$\boldsymbol{a_0} = (\cos\theta, 0, \sin\theta), \quad \text{and} \quad \boldsymbol{g_0} = (0, \sin\theta, \cos\theta). \tag{44}$$

This choice of fiber directions can be either orthogonal or non-orthogonal ($\boldsymbol{a_0} \cdot \boldsymbol{g_0} = \sin\theta \cos\theta$) depending on θ. Figure 5 compares the simulation versus theoretical results for a compression test. By varying θ, our choice of $\boldsymbol{a_0}$ and $\boldsymbol{g_0}$ sweep the fiber families through the XZ- and YZ-planes, respectively. This figure also shows excellent agreement between the theoretically predicted response and the simulation results.
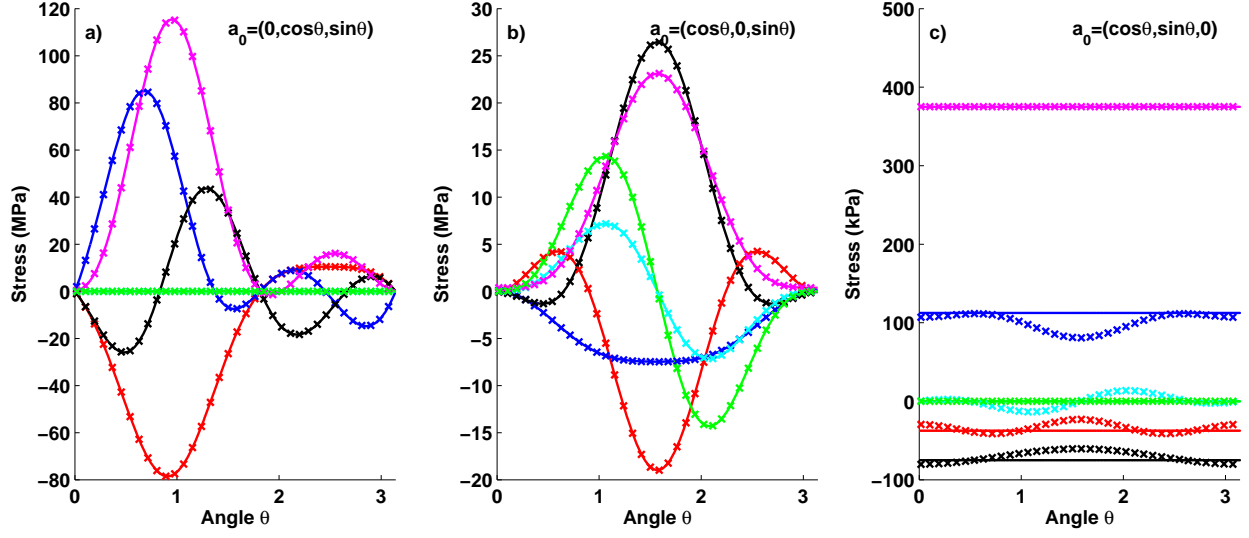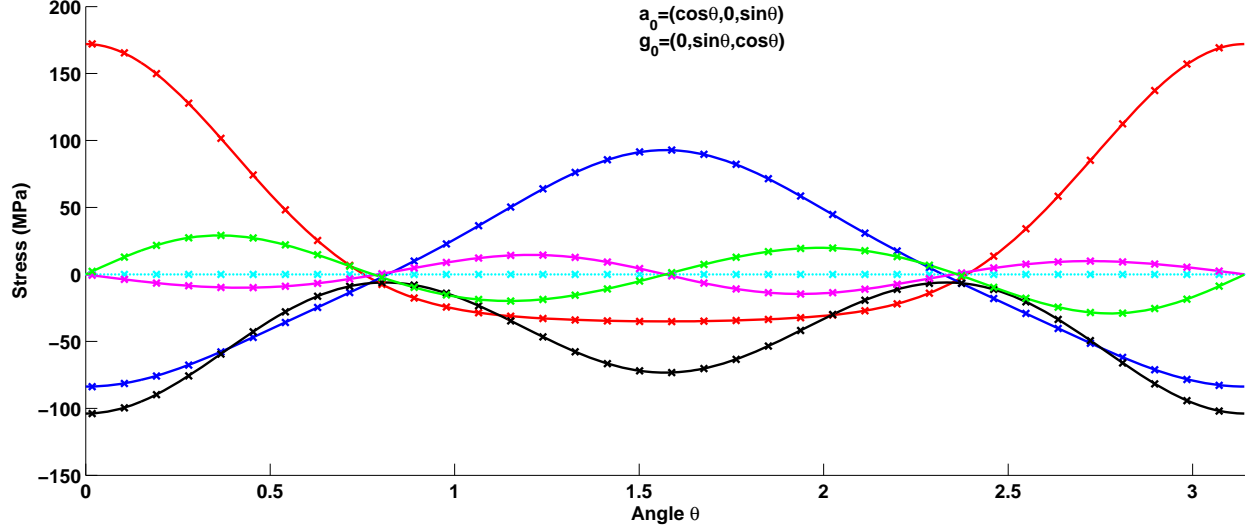
Figure 5. Two fiber families compression test. Simulation (symbols) comparison against theoretical (solid lines) for the components of the Cauchy stress T_{xx} (red), T_{yy} (blue), T_{zz} (black), T_{xy} (cyan), T_{yz} (magenta), and T_{zx} (green) for two fiber family orientation vectors a_0 and g_0.

5. Determining the Fiber Directions for an Intervertebral Disc

This section discusses the overall approach of how we approximate the fiber family directions within intervertebral discs. We begin with a more mathematical description of the fiber orientations within a simplified intervertebral disc and then discuss details of an algorithm to handle some more general geometries.

Our constitutive model is designed to read in a file that lists the fiber family directions as they change in space. Although this model was designed initially for intervertebral discs, it can in theory be extended to handle a number of other materials that have the same feature of one or two fiber directions, e.g., collagen fibers of the cornea, striated muscle fibers in skeletal muscles, multiple axonal directions within the brain. In each case, the choice of the fiber direction, or the manner in which it is assigned to an element, could vary drastically. Since we typically keep the same mesh from one simulation to another, we separated the calculation of the fiber directions per element into a preprocessing step handled in MATLAB. This choice avoided repeated upfront costs associated with determining where fibers were with respect to a mesh, and enables rapid changes to be made without requiring a recompile of SIERRA.

16

As discussed in section 2, the intervertebral discs are reinforced by collagen fibers in the annulus fibrosus. Figure 1c shows that these fibers typically have a regular arrangement within the lamellae of the annulus fibrosus. To describe these directions, we start by approximating the intervertebral disc as a cylinder, as shown in figure 6. Next, we consider a point on the surface of the cylinder, in the figure this is given by some vector r in the reference frame. This surface corresponds to a single lamellae ring. A surface normal can be defined on the cylinder as $\hat{n}$ for which there is a tangent plane. In this example, we set the tangent vector $\hat{t}$ to be parallel with the Z-axis, however, in general this will not be the case for an intervertebral disc since it will be taken to coincide with the normal to the transverse plane of the intervertebral disc. By definition, the binormal vector is $\hat{b} = \hat{t} \times \hat{n}$. According to the experimental literature (*12, 19*), the two fiber family orientations a_0 and g_0 are perpendicular to the surface normal vector $\hat{n}$ and make an angle θ with the tangent vector, i.e.,

$$a_0 \cdot \hat{n} = 0, \quad a_0 \cdot \hat{t} = \cos\theta_a \tag{45}$$
$$g_0 \cdot \hat{n} = 0, \quad g_0 \cdot \hat{t} = \cos\theta_g \tag{46}$$

and

$$\theta_a = -\theta_g. \tag{47}$$
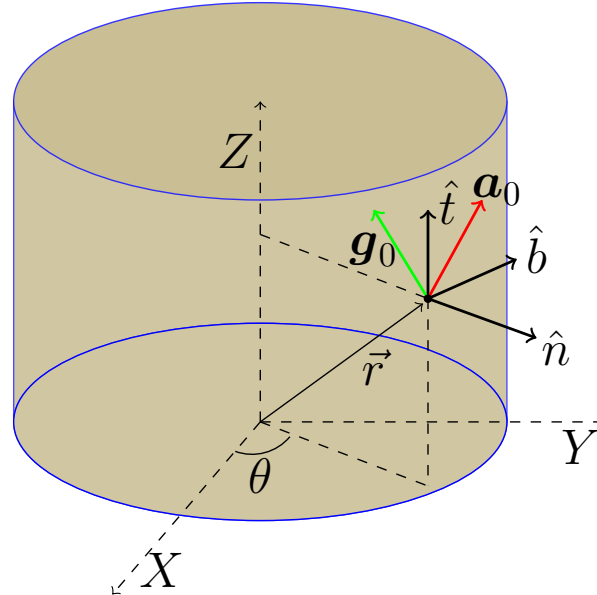
Figure 6. Local coordinate system for an intervertebral disc. An idealized intervertebral disc in the reference coordinate system. The point r is on the surface of the cylinder with corresponding normal vector $\hat{n}$, chosen tangent vector $\hat{t}$, and binormal vector $\hat{b}$. The vectors a_0 and g_0 for this point are also shown.

17

If, in addition to the cylinder shown in figure 6, a second concentric cylinder with a smaller radius is added, it would share the same fiber orientations. The experimental literature describes a similar concentric structure to the orientation of the fiber families in the lamellae rings within the annulus fibrosus. A more generic notion of this concept will be used later when we describe how we determine fiber directions for a specific annulus fibrosus geometry. Thus, if one can determine a surface normal and the tangent vector that is parallel to the intervertebral disc's vertical axis (normal to the transverse plane of the intervertebral disc), then one can calculate the fiber family orientations by applying the appropriate rotations.

To extend the application of these mathematical concepts to a more complicated geometry using a semi-automated approach, the overall procedure is split between two programs: a command line tool and MATLAB.

The first step is handled through a collection of scripts and a tool provided in the SEACAS toolbox that is included with SIERRA, namely "GROPE". This command allows one to manipulate and survey the mesh through the command line and send results to an ASCII file. We used GROPE to extract the centroid location of each element within a given annulus fibrosus and saved it to a delimited file. We use this centroid data as a point-cloud approximation for the actual geometry that we manipulate in MATLAB. A mesh of the spinal segment $L_3L_4L_5$ is shown in figure 7a and a sagittal view of the corresponding point-cloud for a single annulus fibrosus is shown in figure 7b.
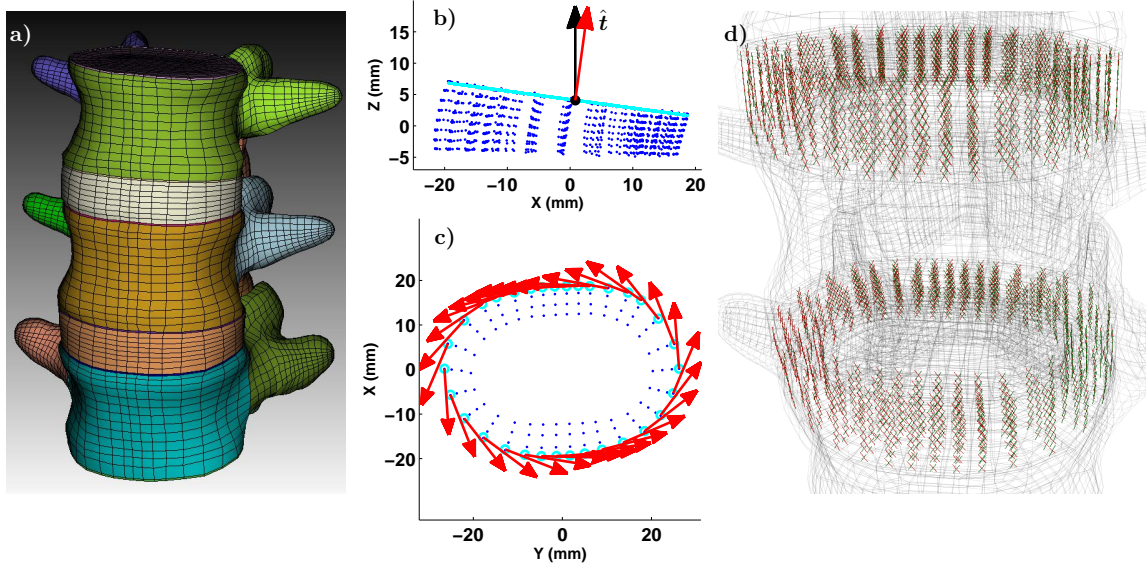
Figure 7. Determining fiber directions in the spine. Panel a is the meshed $L_3L_4L_5$ segment of our spine model. In this drawing, the anterior (forward facing) side corresponds to the Y-axis and the vertical is Z. The centroids of all the elements of the beige intervertebral disc are shown as blue dots in panel b. A linear fit to the top layer of centroids (cyan) gives the slope of that layer. The angle normal to the plane of the intervertebral disc can be determined from this slope (red arrow) relative to the Z-axis (black arrow). This top layer is shown after it is rotated and projected into the XY-plane in panel c. A convex hull algorithm determines the outermost ring of centroids (cyan open circles) from which a parameterization yields the binormal vector $\hat{\boldsymbol{b}}$ (red arrows). Using the angle normal to the plane of the intervertebral disc as the surface tangent vector $\hat{\boldsymbol{t}}$ and the binormal vector from the convex hull $\hat{\boldsymbol{b}}$, the fiber orientations can be determined. Panel d shows a close-up of a wireframe of the original mesh where the calculated two fiber families are shown in red and green.

The algorithm developed in MATLAB is broken into several steps. It is applied to a set of intervertebral discs, but we only discuss its application to a single intervertebral disc.

The first step of the MATLAB code was to simplify the three-dimensional point cloud down to a stack of two-dimensional points. This step is guided by user input so that the centroids of elements that all belonged to the same layer of the mesh could be selected. This simplifying step was only possible because a clear sweep direction of the mesh could be defined. Figure 7b shows that a view of the XZ-plane provides enough space between layers to differentiate them. Each layer of the intervertebral disc is a collection of three-dimensional points that approximately resided in a plane. At this step we made use of another symmetry of the intervertebral discs, the L-R symmetry, which in this case is oriented with the Y-axis. A linear fit of the (X, Z)

19

coordinate points within a single layer gave an approximate slope of that plane (see figure 7b). This slope is then used to obtain a normal vector (red arrow in panel b), which typically fell within 20° of the Z-axis (black arrow). It is important to note that the term "normal vector" refers to the fact that the vector is normal to the plane of the single layer of element centroids. However, in our formulation, this direction actually represents the tangent vector $\hat{t}$ from figure 6 since it is tangent to the surface of the annulus fibrosus. Using the slope, the layer is rotated so that the coordinates of the centroids primarily fell in the XY-plane. With the tangent vector $\hat{t}$ approximately known for this layer, it remains to determine the outward normal $\hat{n}$ or the binormal vector $\hat{b}$. We note that our procedure assumes that the average slope of a layer of elements provides a good estimate for determining the tangent vector $\hat{t}$. However, this will not be the case if the intervertebral disc exhibits large barreling. In this extreme case, additional considerations might be necessary to approximate $\hat{n}$ or $\hat{t}$.

Figure 7c shows the result of rotating and projecting the centroids of the top layer of panel b to the XY-plane. Since the centroids of the annulus fibrosus essentially form a set of elliptical rings in this plane, we use a convex hull algorithm to single out the centroids that belong to the outermost ring (cyan open circles, panel c). Using the coordinates of the outermost ring, a parametric description of the elliptical ring is formed, i.e., $(X(s), Y(s))$. The tangent line of the parametric curve given by $(X(s), Y(s))$ then represents the binormal vector $\hat{b}$, the result of this calculation is shown as the red arrows. This procedure can be repeated by eliminating the outer ring of points and reapplying a convex hull algorithm to identify the next layer of centroids. We emphasize that this algorithm heavily depends on the regularity of our mesh and that other algorithms may be necessary for more complicated meshes or geometries.

The fiber orientations for the full intervertebral disc in the lab frame can be found by using a specific fiber family angle ($\pm\theta$ in figure 6) given relative to the tangent vector $\hat{t}$ (with associated $\hat{b}$ and $\hat{n}$). This is done by working in the reference frame of a single layer of elements in the intervertebral disc, i.e., the slope determined from the single layer is used to obtain X_{disc} and the perpendicular (which corresponds to $\hat{t}$) is our Z_{disc}. We then assign a fiber vector to coincide with Z_{disc}, which in this frame is (0,0,1). The first step is rotating the fiber vector about the Y_{disc}-axis so that it makes an angle θ with the Z_{disc} vector (or $-\theta$ depending on the fiber family). The next rotation accounts for the measured binormal vector $\hat{b}$ for a given element by rotating the resultant vector about the Z_{disc}-axis by the angles represented by the red arrows in figure 7c. The final rotation is to give the single layer of elements the appropriate slope determined earlier by the algorithm. This is accomplished by rotating the resultant vector about the Y_{disc}-axis by the angle between the Z_{disc}-axis and the Z-axis, an angle that was typically less than 20°. The fiber vectors

20

are then translated to the element centroid location, and then translated again to return the annulus fibrosus to coincide with the reference frame.

In practice, this procedure works well for objects whose cross section is convex. The results for two intervertebral discs are shown in figure 7d, which shows a magnified wireframe view of the original mesh. The fiber families are represented by two sets of vectors a_0 (red) and g_0 (green). While this procedure might only approximate experimental data, the strength of our approach is that we can substitute this preprocessing step with actual experimental data in the future.

6.   Future Applications of the Model

This section describes some applications of our transversely isotropic hyperelastic constitutive model with two fiber families. The first example, discussed in section 6.1 presents a preliminary result in modeling an intervertebral disc. The second example, section 6.2, explores the possibility of applying this model to the brain as a continuation of previous research which considered a transversely isotropic hyperelastic constitutive model with a single fiber family. The last two examples explore how the model could be generalized to incorporate a prestress (section 6.3) and an active-contractile element similar to skeletal muscle (section 6.4).

Meshes were generated in Cubit (V13.1; Sandia National Laboratory). Simulations were performed using SIERRA/SolidMechanics (Adagio/Presto 4.28; Sandia National Laboratory). Adagio is an implicit, nonlinear preconditioned conjugate gradient solver and Presto is an explicit solver. Postprocessing of simulation results was carried out in ParaView (V3.14.0; Kitware) and MATLAB (The MathWorks, Natick, MA). Preprocessing the fiber directions was performed using GROPE (SEACAS Toolkit, Sandia National Laboratory), and MATLAB. Additional theoretical calculations were performed using MuPad an application package of MATLAB.

6.1   Modeling Intervertebral Discs

This section briefly covers an example application of our constitutive model applied to the intervertebral discs and compares it against an isotropic Mooney-Rivlin material. We used the algorithm described in section 5 to approximate fiber family directions for a single intervertebral disc surrounded by two vertebrae. In this geometry, the intervertebral disc is tied to the vertebrae. We quasi-statically imposed a displacement to the top vertebra equating to a 1% compressive strain, and fixed the bottom vertebra. This produced a slight barreling, or radial bulging of the intervertebral disc.

The results of our simulations are shown in figure 8. For the transversely isotropic hyperelastic model with two fiber families, we used the material parameters from table 1. The same values were used for the Mooney-Rivlin material with the exception that the fibers were turned off, i.e., $C_a = C_g = 0$. For both material models, the annulus fibrosus was assumed to have a density of 1200 kg/m^3 and the nucleus pulposus had a density of 1000 kg/m^3.
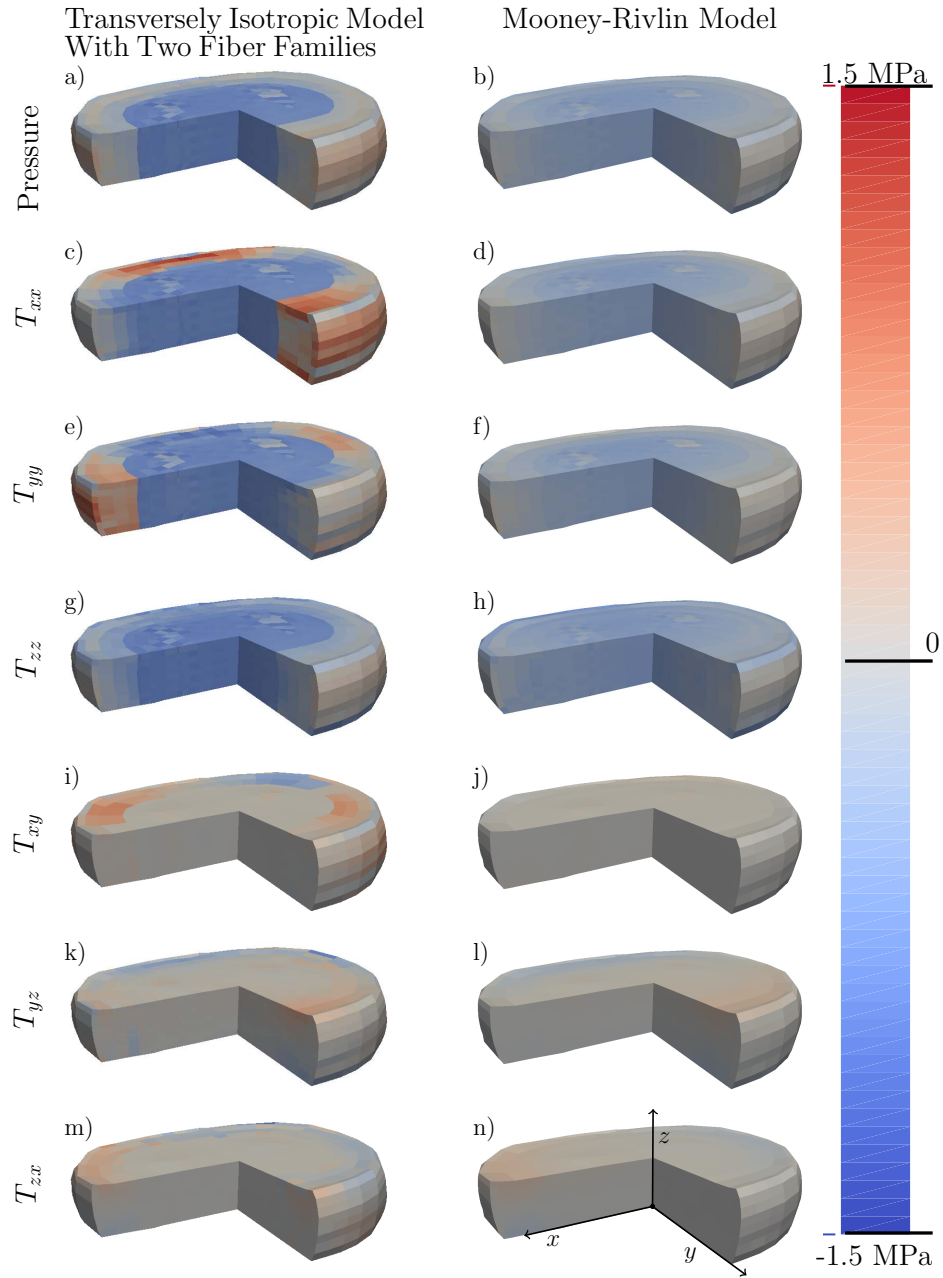
Figure 8. Comparison of constitutive models. Panels a, c, e, g, i, k, and m summarize the simulation results for our transversely isotropic hyperelastic constitutive model with two fiber families. Panels b, d, f, h, j, l, and n are the results of that same material without a fiber response. In both cases, the specimen is subjected to a 1% compressive strain. The resultant pressure, and six components of stress are shown in false color. The orientation of the intervertebral discs relative to a lab coordinate system is shown in panel n and the color bar applies to all panels.

Figure 8 panels a, c, e, g, i, k, and m show the pressure and six components of the Cauchy stress T for the intervertebral disc with the transversely isotropic hyperelastic constitutive model with two fiber families. The panels b, d, f, h, j, l and n show the corresponding pressure and Cauchy stress for the Mooney-Rivlin intervertebral disc. The false color of each of the intervertebral discs is set to the same color scale so that one can directly compare the results of the two models.

As expected, the largest stresses were seen in the annulus fibrosus in the transversely isotropic hyperelastic constitutive model with two fiber families, particularly in the normal stresses T_{xx} and T_{yy} (figure 8c and e), but also in the shear stresses, particularly T_{xy} (figure 8i). The stresses are larger due to the fiber response function, equation 30. For our choice of β, the exponential function is extremely sensitive to any stretch of the fiber family. For a cylinder under uniaxial compression, where the material is allowed to expand radially, we would not expect shear stresses in the Mooney-Rivlin material. However, since the intervertebral discs were tied to the vertebrae, the deformation exhibited a slight barreling, and the original geometry became irregular (see figure 7a), small shear stresses developed even in the Mooney-Rivlin material, e.g., figure 8 panels j, l, and n. These stresses were smaller than those that develop in the transversely isotropic hyperelastic constitutive model with two fiber families (compare panels i and j, panels k and l, or panels m and n). The pressures are larger in the transversely isotropic hyperelastic constitutive model with two fiber families, most notably in the nucleus pulposus (figure 8a). These observations from this preliminary quasi-static simulation appear to support the hypothesis that during dynamic axial compression of the intervertebral disc, the pressure inside the nucleus pulposus increases, forcing the endplates to bulge into the cancellous core of the adjacent vertebra, potentially causing a burst fracture (*26*).

6.2   Modeling Brain Tissue

This section briefly outlines a potential application of our constitutive model to brain tissue. Previously, a transversely isotropic hyperelastic constitutive model with a single fiber family was developed by Kraft and Dagro (*27*) and later used by McKee et al. (*28*). In this model, diffusion spectrum imaging (DSI) was used to provide the constitutive model with the corresponding fiber directions. The experimental data, however, often had more than one unique fiber direction for a given voxel of data. The authors' solution was to provide an average over fiber directions as a first approximation with the intent to extend their model in the future to handle additional fiber families. Using some raw voxel data provided by these authors (*27, 28*), we developed a simple method to extract two fiber directions. Figure 9 presents some example results of this procedure.
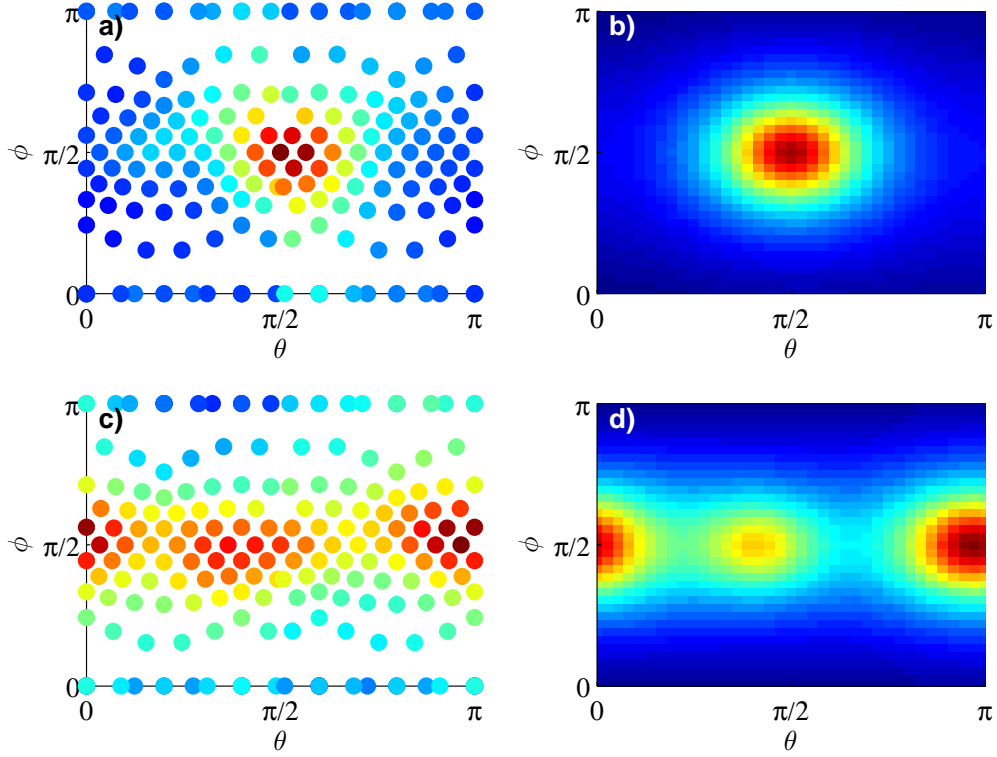
Figure 9. An approach to extract two fiber families from diffusion spectrum imaging (DSI). Panels a and c are the raw data from DSI from two exemplary voxels. The color scale represents the relative strength of the specific direction sampled. The first is a case where there is only a single material direction and the second is a case where there are two material directions. Panels b and d show the result of applying our method to approximate the directions from the raw data.

The measurement received from DSI is a set of voxels that have a set of sampled directions and the associated image intensity in that direction. These data are often represented by a set of unit vectors $\boldsymbol{n}_i$ whose corresponding spherical coordinates are (ρ, θ, ϕ), with:

$$\rho = \sqrt{n_x^2 + n_y^2 + n_z^2} \equiv 1 \,, \quad \theta = \tan^{-1}\left(\frac{n_y}{n_x}\right) \,, \quad \phi = \cos^{-1}\left(n_z\right) \,. \tag{48}$$

In addition to these sample directions is a weight w_i, i.e., the magnitude of the measurement along that sampled direction.

Figure 9a shows the data obtained from a single voxel of DSI. Each filled circle in this panel represents a sampled direction $\boldsymbol{n}_i$ (with some θ_i and ϕ_i). Its color represents the weight w_i or intensity of the DSI measurement in the $\boldsymbol{n}_i$ direction. This particular voxel data shows a case

25

where a single fiber family is present. Figure 9c shows similar data for a case where two distinct fiber directions can be seen. These two cases were chosen to illustrate the importance of improving the average weighting to one that can identify two fiber directions.

We followed the same procedure for both cases to extract the relevant key directions from the raw data. First, we linearly interpolated the DSI data for a single voxel and ran a nonlinear search algorithm ("fminsearch" in MATLAB) to find the maximum intensity and its corresponding pair of angles (θ_0, ϕ_0). After finding the largest peak, we used the Lorentzian function:

$$\frac{\alpha}{\sigma\left[(\theta - \theta_0)^2 + (\phi - \phi_0)^2\right] + 1}, \tag{49}$$

centered at the determined values θ_0 and ϕ_0 to subtract off this peak. For this part of the algorithm, the DSI data are assumed to be π periodic in both θ and ϕ. We chose α from the peak value and used an empirically determined constant value of $\sigma = 0.3$. After performing this subtraction, any negative weights were set to zero, so that upon repeating the entire procedure, the second largest peak could be determined and removed. Determining the two largest peaks in the θ and ϕ interpolated space is equivalent to finding the two sets of angles that best correspond to the two fiber family vectors $\boldsymbol{a}_0$ and $\boldsymbol{g}_0$.

Applying this procedure to the DSI data in figure 9a resulted in a calculated peak at $(\theta_a=1.57, \phi_a=1.57)$. The Lorentzian fit for this first case is shown in figure 9b. Applying the same procedure to the DSI data in figure 9c resulted in two calculated peaks, $(\theta_a=3.03, \phi_a=1.57)$ and $(\theta_g=1.30, \phi_g=1.57)$. The sum of the two Lorentzian functions for the second case is shown in figure 9d. The sets of angles given by θ and ϕ can then be used to determine normal vectors for the two fiber families $\boldsymbol{a}_0$ and $\boldsymbol{g}_0$. It is important to note that the approach used in Kraft and Dagro (27) was to take the weighted average, i.e.,

$$\boldsymbol{a}_0 = \left(\sum_i w_i\right)^{-1} \sum_i \left(w_i(n_x)_i, w_i(n_y)_i, w_i(n_z)_i\right), \tag{50}$$

and enforce that $|\boldsymbol{a}_0| = 1$. To illustrate a potential pitfall of using a weighted average, we also calculated the corresponding weighted average angles $(\theta_a, \phi_a)_{\text{weighted}}$ for these two cases. Using the method from Kraft and Dagro (27), we calculated $(\theta_a, \phi_a)_{\text{weighted}} = (3.03, 1.57)$ for the first case and $(\theta_a, \phi_a)_{\text{weighted}} = (0.04, 1.56)$ for the second case. In the first case, the weighted average does not return a valid representation of the DSI data, since the average is overwhelmed by the low-intensity data. Restricting the average to consider only the stronger weights ($w_i \geq 0.7$) resulted in $(\theta_a, \phi_a)_{\text{weighted}} = (2.15, 1.57)$, which is a much more reasonable result. The potential

26

issue with the method from Kraft and Dagro (*27*) is that the data set is represented by its mean instead of its most probable value. Additionally, in the cases where two fiber families are present, the weighted average cannot pick up on the second peak that is clearly visible in the raw data.

One can attempt to avoid the case of two distinct fiber families by refining the mesh. This was likely the approach in Kraft and Dagro (*27*), where a voxel of DSI data was approximately the same size as an element. However, if a coarser mesh size is used, then the number of DSI voxels contained within an element would increase. The odds of finding multiple fiber families within an element would then also increase. The use of a coarse mesh and two fiber families enables one to capture the mechanical features that the anisotropy introduces and also benefits from a larger time step in an explicit code.

6.3 Incorporating Fiber Prestresses

This section describes how one could accomplish adding a prestress to the fiber families through their stretches. Solvers, like SIERRA, typically assume that the configuration read into the program (in the form of the mesh) is the undeformed reference configuration. In the human body, however, the geometry of an intervertebral disc or a muscle captured from imaging, may not be the "elastically neutral" or stress-free reference configuration. It is reasonable to assume that there would be stresses present at the very beginning of the simulation, e.g., intervertebral discs supporting the weight of the upper body, or tensed or stretched muscles.

As before, let $\boldsymbol{F}$ be the deformation gradient from a reference configuration which has no stress. Let lower case coordinates denote the current configuration (x, y, z), and upper case coordinates (X, Y, Z) denote the reference. Then the deformation gradient is a linear transformation $\boldsymbol{F} : (X, Y, Z) \to (x, y, z)$. Assume also that there is a second reference configuration where the stresses are not necessarily zero. The deformations present in this configuration would correspond to the current mesh that is sent to a simulation. Let the coordinates of this configuration be represented by uppercase with primes $(X'Y'Z')$. We can think of a deformation gradient that takes us from the reference configuration to the configuration read into a simulation as, $\boldsymbol{F}' : (X, Y, Z) \to (X', Y', Z')$. The simulation calculates a rotation matrix and left stretch tensor relative to the primed configuration $(X'Y'Z')$, and so we can also think of a third deformation gradient $\boldsymbol{F}_s : (X', Y', Z') \to (x, y, z)$ (subscript s for simulation). These deformation gradients are related by the following expression:

$$\boldsymbol{F} = \boldsymbol{F}_s \boldsymbol{F}' . \tag{51}$$

Now we consider a fiber family whose direction in the reference configuration is given by $\boldsymbol{a}_0$,

where $|\boldsymbol{a}_0| = 1$. We can again think of the deformed fiber in the current configuration:

$$\boldsymbol{a} = \boldsymbol{F}\boldsymbol{a}_0 = \boldsymbol{F}_s\boldsymbol{F}'\boldsymbol{a}_0 \tag{52}$$

and its associated stretch (which we will need for our fiber response function) is still given by

$$\lambda_a = \frac{\sqrt{\boldsymbol{a}^T\boldsymbol{a}}}{\sqrt{\boldsymbol{a_0}^T\boldsymbol{a_0}}} = \sqrt{\boldsymbol{a_0}^T\boldsymbol{C}\boldsymbol{a_0}}\,. \tag{53}$$

From equation 52, we define an intermediate fiber $\boldsymbol{a}'$ in the primed configuration with the properties that

$$\boldsymbol{a}' = \boldsymbol{F}'\boldsymbol{a}_0\,, \quad \boldsymbol{a} = \boldsymbol{F}_s\,\boldsymbol{a}'\,. \tag{54}$$

We can also define stretches of a fiber in the primed configuration relative to the other configurations. Let λ' denote the stretch of the primed fiber $\boldsymbol{a}'$ relative to the reference configuration $\boldsymbol{a}_0$:

$$\lambda' = \frac{\sqrt{\boldsymbol{a}'^T\boldsymbol{a}'}}{\sqrt{\boldsymbol{a_0}^T\boldsymbol{a_0}}} = \sqrt{\boldsymbol{a_0}^T\boldsymbol{C}'\boldsymbol{a_0}}\,, \tag{55}$$

and let λ_s denote the fiber stretch of the current configuration $\boldsymbol{a}$ relative to the primed configuration $\boldsymbol{a}'$:

$$\lambda_s = \frac{\sqrt{\boldsymbol{a}^T\boldsymbol{a}}}{\sqrt{\boldsymbol{a}'^T\boldsymbol{a}'}} = \frac{\sqrt{\boldsymbol{a}'^T\boldsymbol{C}_s\boldsymbol{a}'}}{\sqrt{\boldsymbol{a}'^T\boldsymbol{a}'}} = \frac{\sqrt{\boldsymbol{a}^T\boldsymbol{a}}}{\sqrt{\boldsymbol{a_0}^T\boldsymbol{a_0}}}\frac{\sqrt{\boldsymbol{a_0}^T\boldsymbol{a_0}}}{\sqrt{\boldsymbol{a}'^T\boldsymbol{a}'}} = \frac{\lambda_a}{\lambda'}\,. \tag{56}$$

These are related by

$$\lambda_a = \lambda_s\lambda'\,. \tag{57}$$

Again, λ_a is the fiber stretch that results in our final deformed configuration and that determines the fiber response, λ' is the initial stretch at the start of the simulation, and λ_s is the additional stretch in the current configuration relative to the primed configuration.

The right Cauchy-Green deformation tensor from the simulation, $\boldsymbol{C}_s$, is calculated by SIERRA during the simulation. This means that $\boldsymbol{a}'$ would need to be determined at the initial run time. Our current method for determining the fiber family orientations uses the primed coordinate system, so the current algorithm determines a reasonable $\boldsymbol{a}'$ direction, but with an unknown magnitude, since we are requiring that $|\boldsymbol{a}_0| = 1$ and thus in general $|\boldsymbol{a}'| \neq 1$. In other words, if we express the Cartesian coordinates of $\boldsymbol{a}'$ relative to a spherical coordinate system,

$$\boldsymbol{a}' = (\lambda'\cos\theta\sin\phi, \lambda'\sin\theta\sin\phi, \lambda'\cos\phi) = \lambda'\hat{\boldsymbol{a}}'\,, \tag{58}$$

our algorithm determines the angles θ and ϕ but λ' is unknown. Thus, if we assume some $\boldsymbol{F}'$, we can formulate the following constraint to determine λ':

$$|\boldsymbol{a}_0| = \sqrt{\boldsymbol{a}_0^T \boldsymbol{a}_0} = \sqrt{\boldsymbol{a}'^T (\boldsymbol{F}'^{-1})^T \boldsymbol{F}'^{-1} \boldsymbol{a}'} = 1\,. \tag{59}$$

Then we could use the following expressions to calculate λ_a:

$$\lambda_a = \sqrt{\boldsymbol{a_0}^T \boldsymbol{C} \boldsymbol{a_0}} = \sqrt{\boldsymbol{a_0}^T \boldsymbol{F}'^T \boldsymbol{C}_s \boldsymbol{F}' \boldsymbol{a_0}}\,. \tag{60}$$

A simpler alternative is to assume we have an idea of λ', then we only need to calculate λ_s to determine λ_a:

$$\lambda_s = \frac{\sqrt{\boldsymbol{a}^T \boldsymbol{a}}}{\sqrt{\boldsymbol{a}'^T \boldsymbol{a}'}} = \frac{\sqrt{\boldsymbol{a}'^T \boldsymbol{C}_s \boldsymbol{a}'}}{\sqrt{\boldsymbol{a}'^T \boldsymbol{a}'}} = \frac{\sqrt{\lambda' \hat{\boldsymbol{a}}'^T \boldsymbol{C}_s \lambda' \hat{\boldsymbol{a}}'}}{\sqrt{\lambda' \hat{\boldsymbol{a}}'^T \lambda' \hat{\boldsymbol{a}}'}} = \sqrt{\hat{\boldsymbol{a}}'^T \boldsymbol{C}_s \hat{\boldsymbol{a}}'}\,. \tag{61}$$

The primed fiber direction $\hat{\boldsymbol{a}}'$ is already determined by the pre-existing algorithm, and SIERRA provides $\boldsymbol{C}_s$, which would play the role of $\boldsymbol{C}$ from section 3. This leaves only the user to choose λ' to introduce a nondimensional scaling to the fiber stretch and amend the implementation of the fiber response function, equation 30, $\mathcal{F}$ so that λ_s is multiplied by the input parameter λ', i.e., $I_4 = (\lambda_s \lambda')^2$.

6.4 Incorporation of Active Contractile Fiber Response

In the previous section, we discussed a method to introduce a prestress to the fiber families. In this section, we briefly discuss how other choices for the fiber response can achieve a variety of new behaviors, such as developing a simple constitutive model for skeletal muscles. Skeletal muscle has been implemented in a variety of ways (29–31). However, a simple implementation that captures the key features of skeletal muscle will be useful to evaluate whether such a model (or more complicated model) is needed in the first place.

The fundamental feature we introduce is that in lieu of a constant function $\mathcal{F}(\lambda_a)$, the fiber response is allowed to dynamically evolve. As such, we present physical arguments that will ultimately lead to an equation of motion describing the dynamic evolution of the fiber response given by $\dot{\mathcal{F}}$. One early model for muscle was developed by A. V. Hill in 1938 (32). A description of Hill's model appears in chapter 18 of the textbook by Keener and Sneyd (33), the key components are only summarized here. The starting point of this model is the notion of an elastic element in series with a contractile element. As such, the length of a muscle fiber L is

decomposed into an elastic component x and a contractile element l so that quite simply,

$$L = l + x \,. \tag{62}$$

By convention, the velocity of the contractile element is given by the negative time derivative of l,

$$v = -\frac{\mathrm{d}l}{\mathrm{d}t} \,. \tag{63}$$

Numerous experiments support a force-velocity relationship between the velocity of shortening v and the load f:

$$(f + a)\,v = b\,(f_0 - f) \,. \tag{64}$$

Here a and b are parameters to be fit by the model and f_0 is the isometric force, the force generated when the muscle length is held fixed. We note that a has dimensions of force and b has dimensions of velocity.

Assuming the force f is a function of the elastic length x, i.e., $F(x)$, we can express the time derivative of f as

$$\dot{f} = \frac{\mathrm{d}F}{\mathrm{d}x}\frac{\mathrm{d}x}{\mathrm{d}t} = \frac{\mathrm{d}F}{\mathrm{d}x}\left[\frac{\mathrm{d}L}{\mathrm{d}t} - \frac{\mathrm{d}l}{\mathrm{d}t}\right] \,, \tag{65}$$

and after inserting the force-velocity relationship, equation 64, into equation 65, we obtain

$$\dot{f} = \frac{\mathrm{d}F}{\mathrm{d}x}\left[\frac{\mathrm{d}L}{\mathrm{d}t} + b\frac{f_0 - f}{f + a}\right] \,. \tag{66}$$

Following the Hill model, F is taken to be a linear function of x, so that

$$F(x) = \alpha\,(x - x_0) \,, \tag{67}$$

where α is some elastic spring coefficient. This gives us the Hill model for active contractile muscle fibers:

$$\dot{f} = \alpha\left[\frac{\mathrm{d}L}{\mathrm{d}t} + b\frac{f_0 - f}{f + a}\right] \,. \tag{68}$$

At this point, we introduce a possible extension of our model to include this behavior. If, instead of considering forces, we consider stresses, then we can modify equation 68. This modified equation can then be taken to directly affect the fiber response function $\mathcal{F}$. By letting $f \to \mathcal{F}$, $\alpha \to C$, $b \to \beta$ and $L \to \lambda_a$, we come to the following result:

$$\dot{\mathcal{F}} = C\left[\dot{\lambda}_a + \beta\frac{\mathcal{F}_0 - \mathcal{F}}{\mathcal{F} + a}\right] \,. \tag{69}$$

30

C and a have units of stress and $\dot{\lambda}_a$ and β are strain-rates, e.g., 1/s. This is now an equation that governs the functional dependence of the fiber response that is qualitatively consistent with a Hill-type muscle law. At each time step, the task is then to calculate the muscle fiber stretch λ_a and its time derivative $\dot{\lambda}_a$ so that the fiber response $\mathcal{F}$ at the current time step can be calculated. One possible discretization of this is (first order, forward time):

$$\mathcal{F}^{n+1} = \mathcal{F}^n + C\left(\lambda_a^{n+1} - \lambda_a^n\right) + C\beta\frac{\mathcal{F}_0^n - \mathcal{F}^n}{\mathcal{F}^n + a}\,\Delta t\,, \tag{70}$$

where the superscript n denotes the time step at which the variable is evaluated. While this is not a rigorous approach to incorporating a fiber response that mimics skeletal muscle, it is an outline of an approach that could be made rigorous in future studies.

7. Concluding Remarks

We have developed and verified a transversely isotropic hyperelastic constitutive model with two fiber families that can readily be applied to soft biological tissues exhibiting anisotropic features. We have outlined some current projects involving the applications of this model, specifically regarding the spine. In addition, we presented a clear pathway on how to alter the preprocessing step so that this model can be used with DSI data from brain tissue to capture a second fiber direction. Finally, we outlined a general procedure of how the fiber response could be easily modified to represent prestress and active-contractile muscle behavior.

8. References

1. El-Rich, M.; Arnoux, P.-J.; Wagnac, E.; Brunet, C.; Aubin, C.-E. Finite Element Investigation of the Loading Rate Effect on the Spinal Load-Sharing Changes Under Impact Conditions. *Journal of Biomechanics* **2009**, *42*, 1252–1262.

2. Untaroiu, C.; Darvish, K.; Crandall, J.; Deng, B.; Wang, J.-T. Characterization of the Lower Limb Soft Tissues in Pedestrian Finite Element Models. In *Proceedings of 19th ESV Conference*, Washington DC, 2005.

3. Stitzel, J. D.; Duma, S. M.; Cormier, J. M.; Herring, I. P. A Nonlinear Finite Element Model of the Eye With Experimental Validation for the Prediction of Globe Rupture. *Stapp Car Crash Journal* **2002**, *46*, 81–102.

4. Kraft, R. H.; Lynch, M. L.; Vogel, E. W., III. Computational Failure Modeling of Lower Extremities. In *Proceedings of the NATO HFM-207 Symposium*, Halifax, Canada, 2011.

5. Shuck, L.; Advani, S. Rheological Response of Human Brain Tissue in Shear. *Journal of Basic Engineering* **1972**, *94*, 905.

6. Miller, K.; Chinzei, K. Constitutive Modelling of Brain Tissue: Experiment and Theory. *Journal of Biomechanics* **1997**, *30* (11), 1115–1121.

7. Donnelly, B.; Medige, J. Shear Properties of Human Brain Tissue. *Journal of Biomechanical Engineering* **1997**, *119* (4), 423–432.

8. Nicolle, S.; Lounis, M.; Willinger, R. Shear Properties of Brain Tissue Over a Frequency Range Relevant for Automotive Impact Situations: New Experimental Results. *Stapp Car Crash Journal* **2004**, *48*, 239.

9. Hrapko, M.; Van Dommelen, J.; Peters, G.; Wismans, J. The Mechanical Behaviour of Brain Tissue: Large Strain Response and Constitutive Modelling. *Biorheology* **2006**, *43* (5), 623–636.

10. Saraf, H.; Ramesh, K.; Lennon, A.; Merkle, A.; Roberts, J. Measurement of the Dynamic Bulk and Shear Response of Soft Human Tissues. *Experimental Mechanics* **2007**, *47* (3), 439–449.

11. de Jager, M. *Mathematical Modelling of the Human Cervical Spine: A Survey of the Literature*; Internal Report WFW-93.027; Eindhoven University of Technology: The Netherlands, 1993.

12. Raj, P. P. Intervertebral Disc: Anatomy-Physiology-Pathophysiology-Treatment. *Pain Practice* **2008**, *8* (1), 18–44.

13. Pezowicz, C. Analysis of Selected Mechanical Properties of Intervertebral Disc Annulus Fibrosus in Marco and Microscopic Scale. *Journal of Theoretical and Applied Mechanics* **2010**, *48* (4), 917–932.

14. Shirazi-Adl, A. On the Fibre Composite Material Models of Disc Annulus – Comparison of Predicted Stresses. *Journal of Biomechanics* **1989**, *22* (4), 357–365.

15. Moore, R. The Vertebral End-Plate: What Do We Know? *European Spine Journal* **2000**, *9* (2), 92–96.

16. Kraft, R. H.; Wozniak, S. L. *A Review of Computational Spinal Injury Biomechanics Research and Recommendations for Future Efforts*; ARL-TR-5673; U.S. Army Research Laboratory: Aberdeen Proving Ground, MD, 2011.

17. Rao, A.; Dumas, G. Influence of Material Properties on the Mechanical Behaviour of the L_5-S_1 Intervertebral Disc in Compression: A Nonlinear Finite Element Study. *Journal of Biomedical Engineering* **1990**, *13*, 139–151.

18. Kim, H. J.; Chun, H. J.; Kang, K. T.; Lee, H. M.; Kim, H. S.; Moon, E. S.; Park, J. O.; Hwang, B. H.; Son, J. H.; Moon, S. H. A Validated Finite Element Analysis of Nerve Root Stress in Degenerative Lumbar Scoliosis. *Medical & Biological Engineering & Computing* **2009**, *47*, 599–605.

19. Lee, C. K.; Kim, Y. E.; Lee, C. S.; Hong, Y. M.; Jung, J. M.; Goel, V. K. Impact Response of the Intervertebral Disc in a Finite-Element Model. *Spine* **2000**, *25* (19), 2431–2439.

20. Mascio, V.; Bellini, C.; Galbusera, F.; Raimondi, M.; Brayda-Bruno, M.; Assietti, R. Lumbar Total Disc Replacement: A Numerical Study. *Journal of Applied Biomaterials & Biomechanics* **2010**, *8* (2), 97–101.

21. Holzapfel, G. A. Biomechanics of Soft Tissue. In *The Handbook of Materials Behavior Models*; Academic Press: San Diego, CA, 2001; Volume. 3, pp 1049–1063.

22. Weiss, J. A.; Maker, B. N.; Govindjee, S. Finite Element Implementation of Incompressible, Transversely Isotropic Hyperelasticity. *Computer Methods in Applied Mechanics and Engineering* **1996**, *135* (1), 107–128.

23. Holzapfel, G. A. *Nonlinear Solid Mechanics*; John Wiley & Sons, Chichester: 2000.

24. Pinsky, P. M.; van der Heide, D.; Chernyak, D. Computational Modeling of Mechanical Anisotropy in the Cornea and Sclera. *Journal of Cataract & Refractive Surgery* **2005**, *31* (1), 136–145.

25. Nguyen, T.; Boyce, B. An Inverse Finite Element Method for Determining the Anisotropic Properties of the Cornea. *Biomechanics and Modeling in Mechanobiology* **2011**, *10* (3), 323–337.

26. Qui, T.-X.; Tan, K.-W.; Lee, V.-S.; Teo, E.-C. Investigation of Thoracolumbar T12-L1 Burst Fracture Mechanism Using Finite Element Method. *Medical Engineering & Physics* **2006**, *28*, 656–664.

27. Kraft, R. H.; Dagro, A. M. *Design and Implementation of a Numerical Technique to Inform Anisotropic Hyperelastic Finite Element Models Using Diffusion-Weighted Imaging*; ARL-TR-5796; U.S. Army Research Laboratory: Aberdeen Proving Ground, MD, 2011.

28. McKee, P. J.; Dagro, A. M.; Vindiola, M. M.; Vettel, J. M. *Fiber Segment-Based Degradation Methods for a Finite Element-Informed Structural Brain Network*; ARL-TR-6739; U.S. Army Research Laboratory: Aberdeen Proving Ground, MD, 2013.

29. Johansson, T.; Meier, P.; Blickhan, R. A Finite-Element Model for the Mechanical Analysis of Skeletal Muscles. *Journal of Theoretical Biology* **2000**, *206* (1), 131–149.

30. Blemker, S. S.; Delp, S. L. Three-Dimensional Representation of Complex Muscle Architectures and Geometries. *Annals of Biomedical Engineering* **2005**, *33* (5), 661–673.

31. Ehret, A. E.; Böl, M.; Itskov, M. A Continuum Constitutive Model for the Active Behaviour of Skeletal Muscle. *Journal of the Mechanics and Physics of Solids* **2011**, *59* (3), 625–636.

32. Hill, A. V. The Heat of Shortening and the Dynamic Constants of Muscle. *Proceedings of the Royal Society of London. Series B, Biological Sciences* **1938**, *126* (843), 136–195.

33. Keener, J.; Sneyd, J. *Mathematical Physiology*; Springer-Verlag New York: 2008.

NO. OF COPIES	ORGANIZATION
4 (PDF)	DIR USARL RDRL DPW R COATES P FROUNFELKER R SPINK M TEGTMEYER
1 (PDF)	DIR USARL RDRL ROP L F GREGORY
2 (PDF)	DIR USARL RDRL CIH C B HENZ M VINDIOLA
10 (PDF)	DIR USARL RDRL HR P FRANASZCZUK RDRL HRS C S GORDON W HAIRSTON B LANCE K MCDOWELL J MCARDLE K OIE A PASSARO M PETERSON J VETTEL
9 (PDF)	DIR USARL RDRL SLB W D BOOTHE A BREUER N EBERIUS G ETTIENNE-MODESTE P GILLICH C KENNEDY A KULAGA M MENTZER W MERMAGEN

NO. OF COPIES	ORGANIZATION
45 (PDF)	DIR USARL RDRL WM S KARNA RDRL WML C T PIEHLER RDRL WML H B SCHUSTER RDRL WMM B B LOVE RDRL WMM G L PIEHLER N ZANDER RDRL WMP S SCHOENFELD RDRL WMP B A DAGRO A DILEONARDI A DWIVEDI W EVANS C GUNNARSSON C HOPPEL Y HUANG M LYNCH J MCDONALD P MCKEE D POWELL B SANBORN S SATAPATHY A SOKOLOW C WEAVER T WEERASOORIYA S WOZNIAK T ZHANG K ZIEGLER RDRL WMP C S BILYK T BJERKE D CASEM J CLAYTON D DANDEKAR M GREENFIELD B LEAVY M RAFTENBERG RDRL WMP D R DONEY J RUNYEON RDRL WMP E P SWOBODA RDRL WMP F E FIORAVANTE A FRYDMAN

NO. OF
COPIES   ORGANIZATION

        N GNIAZDOWSKI
        R GUPTA
        R KARGUS
     RDRL WMP G
        R BANTON
        N ELDREDGE
        S KUKUCK

INTENTIONALLY LEFT BLANK.